Optik - International Journal for Light and Electron Optics 217 (2020) 164808

Contents lists available at ScienceDirect

Optik

journal homepage: www.elsevier.com/locate/ijleo

Original research article

Machine learning optical band gaps of doped-ZnO films

Yun Zhang*, Xiaojie Xu

North Carolina State University, Raleigh, NC 27695, USA

ARTICLE INFO

Keywords:
Zinc oxide
Optical property
Machine learning
Lattice constant
Grain size
Bandgap
Gaussian process regression

ABSTRACT

Tailoring the optical bandgap, E_g, of ZnO nanostructured thin films is of great interest to meet increasing demands for diverse practical applications, such as optoelectronics, spintronics, and photonics. Processing parameters, dopant selection, and various combinations of the two have significant effects on the crystal structure and microstructure of fabricated films, and thus optical performance. Empirical results and previous models through the first principle show that changes in lattice parameters and the grain size correlate with those in E_g. But correlations are complicated and the models rarely apply to complex situations such as co-doped films. In this work, the Gaussian process regression (GPR) model is developed to elucidate the statistical relationship among the lattice parameters, grain size, and energy bandgap for doped-ZnO films. A total of 65 ZnO films with E_g ranging from 2.100 eV to 3.760 eV are explored. The modeling approach demonstrates a high degree of accuracy and stability, contributing to efficient and low-cost estimations of E_g.

1. Introduction

Zinc oxide (ZnO), an intrinsic n-type semiconductor, has attracted much attention recently in application areas, including photonics, spintronics, and optoelectronics, due to its outstanding physical properties, such as a wide bandgap, E_g (~3.36 eV), high exciton binding energy (~60 meV), high redox potential, and high chemical stability. In particular, ZnO nanostructured films are much more preferred in devices, such as transparent conductive oxide thin films in solar cells, piezoelectric devices, optoelectronic switches, laser diodes, light emitting diodes, surface acoustic wave guides, and gas sensors [8,10,17,27,28,30,33].

Due to requirements of optical and electronic properties in different practical applications, extensive research has been conducted to tailor E_g along with other physical properties, such as electrical conductivity and transmittance. For undoped-ZnO films, structural, optical, and electrical properties are varied by using different synthesis methods. Most ZnO films are nanocrystalline films with a hexagonal wurtzite structure, which has a strong (002) preferred orientation. There is a wide variety of methods to fabricate ZnO films, such as the sol-gel process, spray pyrolysis, molecular beam epitaxy, chemical vapor deposition, and magnetron sputtering [3,7,18]. Processing parameters, including but not limited to, precursor materials, substrate temperature, deposition rates, annealing temperature, and substrate types, affect the crystal structure and microstructure of fabricated films significantly. As a result, the lattice parameters, grain size, and residual strain are changed upon different combinations of synthesis steps [16,22,24,34–36]. For example, increases in the grain size are reported to contribute to quantum confinement effects, which result in decreases of E_g [3]. The texture of ZnO films also depends on the substrate type and structure [18]. Due to the lattice mismatch and strain, E_g's of similarly fabricated ZnO films on the bare glass, ITO coated glass, and ZnO:Al substrates are different. Another widely adopted way to alter the ZnO bandgap is chemical doping as it can shift the fermi level and create impurity states [2]. Both single doping and co-

* Corresponding author.
E-mail addresses: yzhang43@ncsu.edu (Y. Zhang), xxu6@ncsu.edu (X. Xu).

https://doi.org/10.1016/j.ijleo.2020.164808
Received 16 March 2020; Received in revised form 7 April 2020; Accepted 25 April 2020

Table 1
Experimental data and predictions.

Sample	a (Å)	c (Å)	Grain size (nm)	E_g (eV)	Prediction	Reference
CdS-doped ZnO	3.31000	5.36000	36.81	2.100	2.10008	[29]
10% Cu-doped ZnO at 700 °C	3.24600	5.19900	150.00	2.640	2.64006	[12]
$Zn_{0.85}Ni_{0.15}O$	3.22700	5.17800	14.00	2.870	2.87010	[9]
$Zn_{0.90}Ni_{0.01}O$	3.23100	5.18400	13.00	2.940	2.94008	[9]
2 wt% Ag-doped ZnO	3.25100	5.20800	382.00	2.970	2.97001	[1]
1 wt% Ag-doped ZnO	3.25000	5.20500	357.00	2.980	2.98001	[1]
ZnO/glass	3.25800	5.20800	32.00	3.020	3.02005	[18]
$\mathbf{Zn_{0.96}Ni_{0.04}}O$	3.22700	5.17800	11.00	3.030	3.02996	[9]
Al-doped ZnO D	3.32600	5.29200	15.01	3.080	3.08001	[14]
0.5 wt% Ag-doped ZnO	3.24900	5.20200	260.00	3.110	3.11000	[1]
Al-doped ZnO B	3.35900	5.32200	20.83	3.110	3.11001	[14]
Al-doped ZnO C	3.33900	5.30200	17.93	3.120	3.12000	[14]
$Zn_{0.98}Ni_{0.02}O$	3.22700	5.17200	16.00	3.150	3.15002	[9]
ZnO/ITO/glass	3.27900	5.19800	33.00	3.180	3.18000	[18]
Undoped ZnO	3.31000	5.36000	67.31	3.180	3.17998	[29]
0.25 wt% Ag-doped ZnO	3.22900	5.17900	218.00	3.190	3.19000	[1]
Al-doped ZnO A	3.36100	5.32600	22.71	3.200	3.19998	[14]
Undoped ZnO	3.22600	5.16600	180.00	3.210	3.20999	[1]
10% Cu-doped ZnO at 900 °C	3.24500	5.19700	200.00	3.210	3.20999	[12]
5 at% Sn-doped ZnO	3.66000	4.98000	60.04	3.218	3.21800	[5]
0.5 at% Sn-doped ZnO	3.25000	5.21000	45.95	3.237	3.23700	[5]
$Zn_{0.95}Cu_{0.05}O$	3.23000	5.21000	28.74	3.240	3.24004	[4]
Undoped ZnO	3.23090	5.17180	25.80	3.240	3.24002	[11]
0.1 at% Sn-doped ZnO	3.25000	5.21000	52.36	3.245	3.24500	[5]
Undoped ZnO	3.25000	5.21000	50.93	3.246	3.24600	[5]
$Zn_{0.96}Cu_{0.04}O$	3.23000	5.21000	28.52	3.250	3.24996	[4]
ZnO: Ag 3%	3.24090	5.18880	79.24	3.250	3.25002	[13]
0% Li-doped ZnO: 2% Sn	3.25000	5.20700	139.00	3.250	3.24998	[23]
$Zn_{0.97}Cu_{0.03}O$	3.25000	5.21000	27.92	3.250	3.24997	[4]
Undoped ZnO	3.23600	5.18500	50.00	3.260	3.26000	[12]
Undoped ZnO	3.24200	5.20500	113.00	3.260	3.26000	[23]
3% Li-doped ZnO: 2% Sn	3.25300	5.20900	139.00	3.260	3.26000	[23]
Ga-doped ZnO, 10 kGy irradiation dose	2.59800	5.19400	31.05	3.262	3.26200	[25]
Undoped ZnO	3.24337	5.18939	21.91	3.265	3.26506	[3]
1 at% Sn-doped ZnO	3.25000	5.21000	39.23	3.265	3.26498	[5]
Ga-doped ZnO, 5 kGy irradiation dose	2.60000	5.19700	29.62	3.267	3.26700	[25]
Undoped ZnO	3.24572	5.19314	25.03	3.267	3.26700	[6]
Ga-doped ZnO, 1 kGy irradiation dose	2.60100	5.20000	29.40	3.270	3.27000	[25]
ZnO: Ag 2%	3.24420	5.19130	93.23	3.270	3.27003	[13]
2 at% Sn-doped ZnO	3.25000	4.98000	71.84	3.272	3.27199	[5]
Ga-doped ZnO, 0 kGy irradiation dose	2.60300	5.20300	27.83	3.274	3.27400	[25]
2 wt% Al-doped ZnO	3.24372	5.18992	20.40	3.275	3.27501	[6]
Undoped ZnO	3.24064	5.18502	12.41	3.277	3.27695	[3]
Undoped ZnO	3.26815	5.22904	16.01	3.279	3.27899	[3]
Undoped ZnO	3.23248	5.17197	20.29	3.280	3.28000	[3]
0.25 at% Sm-doped ZnO	3.23420	5.17410	26.10	3.280	3.28001	[11]
ZnO: Ag 1%	3.24280	5.18880	89.92	3.280	3.28000	[13]
5% Li-doped ZnO: 2% Sn	3.26400	5.21900	147.00	3.280	3.27999	[23]
3.5 wt% Al-doped ZnO	3.24064	5.18503	24.49	3.283	3.28303	[6]
7% Li-doped ZnO: 2% Sn	3.25300	5.21500	139.00	3.290	3.29000	[23]
Undoped ZnO	3.25730	5.21370	84.30	3.290	3.29001	[13]
2.25 wt% Al-doped ZnO	3.24349	5.18956	21.44	3.296	3.29594	[6]
2 wt% Mg-doped ZnO	3.28200	5.13400	17.05	3.300	3.30000	[19]
3 wt% Al-doped ZnO	3.24337	5.18939	33.28	3.305	3.30500	[6]
2.5 wt% Al-doped ZnO	3.24337	5.18937	26.05	3.311	3.31099	[6]
4 wt% Mg-doped ZnO	3.29100	5.14300	25.95	3.320	3.32000	[19]
2.75 wt% Al-doped ZnO	3.23792	5.18067	29.72	3.325	3.32500	[6]
6 wt% Mg-doped ZnO	3.27600	5.14800	35.93	3.330	3.33000	[19]
8 wt% Mg-doped ZnO	3.27200	5.13100	56.70	3.390	3.38999	[19]
0.50 at% Sm-doped ZnO	3.23650	5.17660	19.60	3.400	3.39995	[11]
1.00 at% Sm-doped ZnO	3.23270	5.18300	19.80	3.410	3.40994	[11]
0.75 at% Sm-doped ZnO	3.23820	5.18020	21.00	3.430	3.42998	[11]
Undoped ZnO	3.21900	5.16600	20.00	3.470	3.46996	[9]
ZnO/ZnO: Al/glass	3.06900	5.20200	39.00	3.540	3.53997	[18]
7% Cu-doped ZnO at 700 °C	3.24500	5.19800	87.50	3.760	3.75993	[12]
Minimum	2.59800	4.98000	11.00	2.100	2.10008	–
Mean	3.21792	5.19666	65.99	3.220	3.22014	–

(*continued on next page*)

Table 1 (*continued*)

Sample	a (Å)	c (Å)	Grain size (nm)	E_g (eV)	Prediction	Reference
Median	3.24420	5.19400	31.05	3.262	3.26200	–
Maximum	3.66000	5.36000	382.00	3.760	3.75993	–
Standard deviation	0.17135	0.05928	77.35	0.208	0.20838	–
Correlation coefficient with E_g	−12.26%	−34.90%	−18.82%	–	99.99%	–

Notes: "E_g (eV)" and "prediction" represent the experimental and GPR predicted band gaps, respectively, which are visualized in Fig. 3.

doping methods have been applied to ZnO film fabrications by incorporating various elements into the crystal structure, i.e. group I elements (Ag and Li), group II elements (Mg), group III elements (B, Ga, In, and Al), transition metals (Cu, Fe, Ni, and Mn), and rare-earth metals (Te and Sm) [1,4–6,9,11–14,19,23,25,26,29]. The alloying show lattice distortions and changes in E_g due to electronegativity and ionic radius differences [19]. Variations in the bond angle and bond length are reflected directly through changes in lattice parameters. Furthermore, the microstructure of films, as characterized by the grain size, shows additional influence on film quality and optical performance. The grain size is correlated with the residual strain, dislocation density, and other structural defects, which is shown to contribute to the weak Burstein-Moss effect [25]. With various synthesis methods and dopant selection, combination possibilities of ZnO films with tunable E_g are enormous. Therefore, it is of great importance to investigate relationships among the tunability of E_g, lattice parameters, and grain size. Qualitative analysis on the effect of dopant types and levels on E_g of ZnO films has been conducted through experiments [1,3–6,9,11–14,18,19,23,25,29]. Quantitative analysis through thermodynamics models and first principle models has been utilized to aid the understanding of optical performance of these materials and facilitate tuning of ZnO E_g for optoelectronic devices [15,20,21,31,32,43]. However, these models require a significant amount of data inputs, such as variables for equations of state and orbital configurations, which can only be obtained by extensive measurements. The requirement on computational power also increases significantly when it comes to the co-doping situation.

In this work, the Gaussian process regression (GPR) model is developed to elucidate the statistical relationship among the lattice parameters, a (Å) and c (Å), grain size, and energy bandgap for doped-ZnO films. The model generalizes well in the presence of a few descriptive features, where intelligent algorithms are able to learn and recognize the patterns. This modeling approach demonstrates a high degree of accuracy and stability, contributing to efficient and low-cost estimations of the energy bandgap of ZnO films and understandings of which based on the lattice parameters and grain size. As one of the computational intelligence techniques, the GPR model has already been utilized in other materials systems to predict significant physical parameters in different fields of applications [37–42]. This model can serve as a guideline for searching for ZnO films with specific E_g's and can be used as part of machine learning to aid understandings of doping and processing effects on optical performance of ZnO films.

The remaining of this work is organized as follows. Section 2 proposes the GPR model. Section 3 describes the data and computational methodology. Section 4 presents and discusses results, and Section 5 concludes.

2. Proposed methodology

2.1. Brief description of Gaussian process regression

GPRs are nonparametric kernel-based probabilistic models. A GPR aims at explaining y by introducing latent variables, $l(x)$'s, from a Gaussian process such that the joint distribution of $l(x)$'s is Gaussian, and explicit basis functions, b. Let $m(x) = E(l(x))$ be the mean function and $k(x, x') = \mathrm{Cov}[l(x), l(x')]$ the covariance function, and consider now the GPR model, $y = b(x)^T\beta + l(x)$, where $l(x) \sim \mathrm{GP}(0, k(x, x'))$ and $b(x) \in \mathbb{R}^p$. $k(x, x')$ is often parameterized by the hyperparameter, θ, and thus might be written as $k(x, x'|\theta)$. In general, different algorithms estimate β, σ^2, and θ for model training and would allow specifications of b and k, as well as initial values for parameters.

The current study explores four kernel functions, namely Exponential, Squared Exponential, Matern 5/2, and Rational Quadratic, whose specifications are listed in Eqs. (1)–(4), respectively, where σ_l is the characteristic length scale defining how far apart x's can be for y's to become uncorrelated, σ_f is the signal standard deviation, $r = \sqrt{(x_i - x_j)^T} \times \sqrt{(x_i - x_j)}$, and α is a positive-valued scale-mixture parameter. Note that σ_l and σ_f should be positive. This could be enforced through θ such that $\theta_1 = \log\sigma_l$ and $\theta_2 = \log\sigma_f$.

$$k(x_i, x_j|\theta) = \sigma_f^2 \exp\left(-\frac{r}{\sigma_l}\right) \tag{1}$$

$$k(x_i, x_j|\theta) = \sigma_f^2 \exp\left[-\frac{1}{2}\frac{(x_i - x_j)^T(x_i - x_j)}{\sigma_l^2}\right] \tag{2}$$

$$k(x_i, x_j|\theta) = \sigma_f^2\left(1 + \frac{\sqrt{5}r}{\sigma_l} + \frac{5r^2}{3\sigma_l^2}\right)\exp\left(-\frac{\sqrt{5}r}{\sigma_l}\right) \tag{3}$$

$$k(x_i, x_j|\theta) = \sigma_f^2\left(1 + \frac{r^2}{2\alpha\sigma_l^2}\right)^{-\alpha} \tag{4}$$

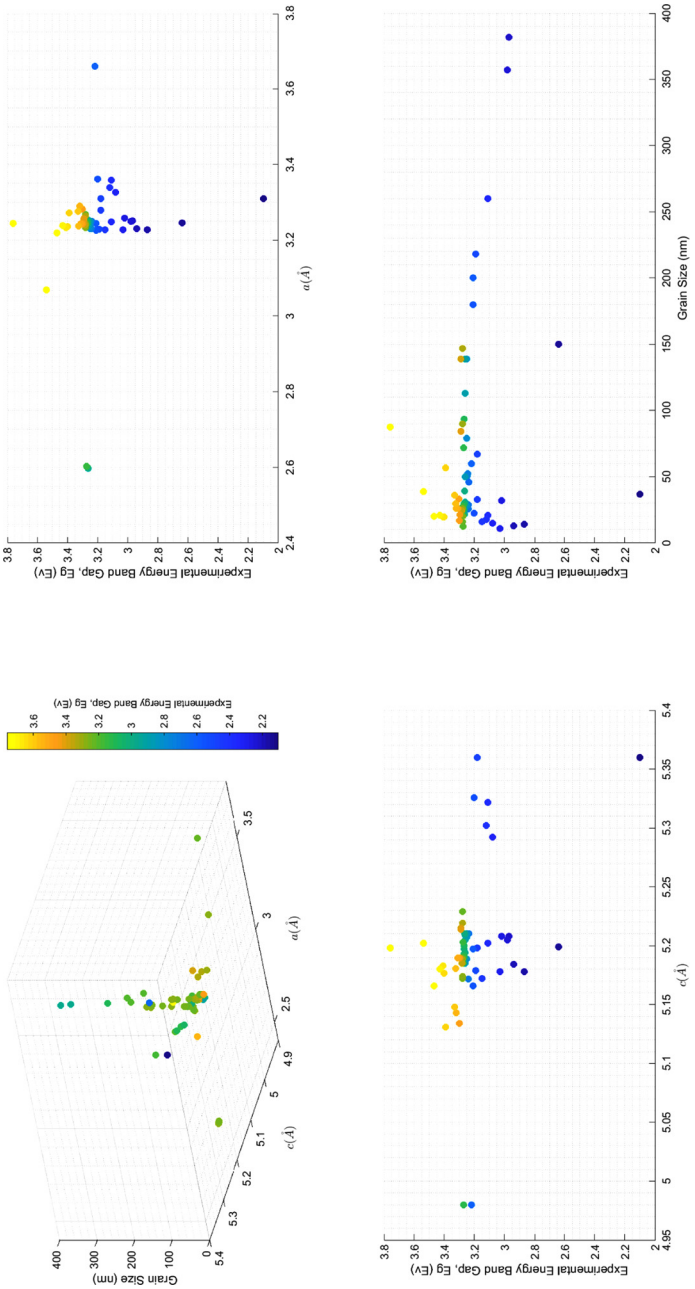

Fig. 1. Data visualization.

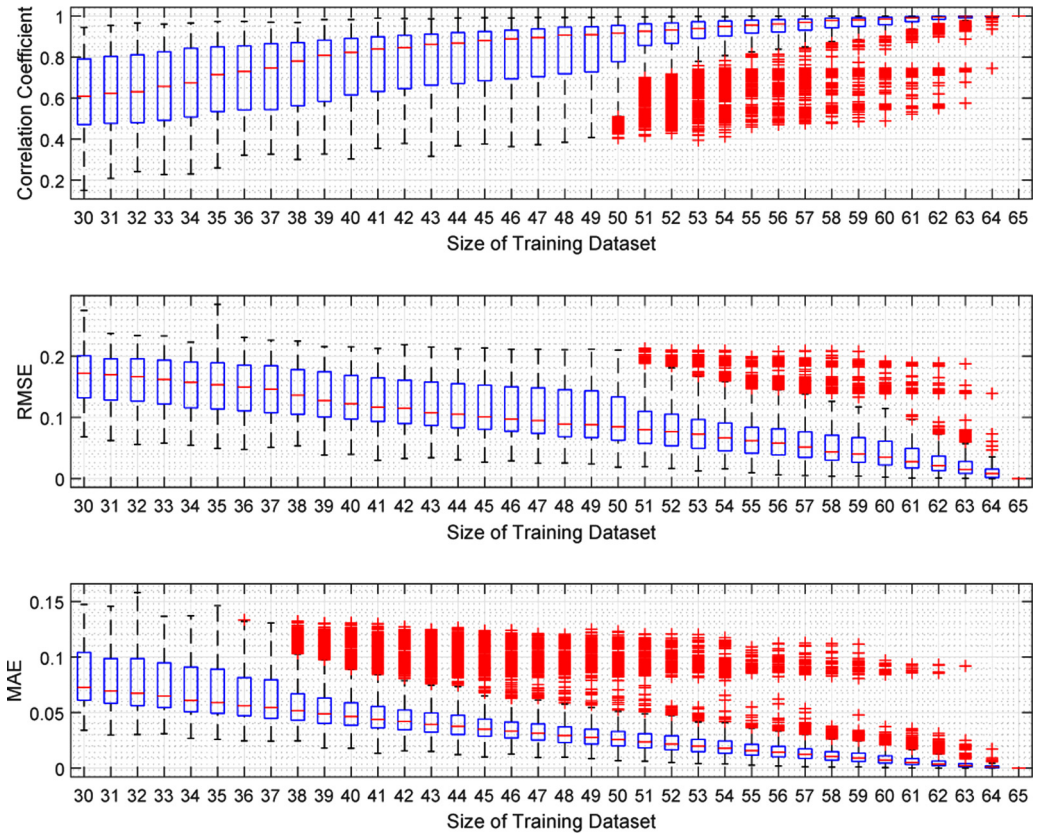

Fig. 2. Model performance and training data sizes. When the training dataset size is between 30 and 63, 2000 random sub-samples are drawn without replacements from the whole sample for model training. When the training dataset size is 64 or 65, ${}_{65}C_{64}$ or ${}_{65}C_{65}$ sub-samples are drawn without replacements from the whole sample based on exhaustive sampling for model training. Each trained model based on a certain sub-sample is used to score the whole sample and obtain the associated model performance. The GPR here uses the Exponential kernel and Constant basis function, with standardized predictors. Given a model performance measure, box plots show the median, 25th percentile, and 75th percentile. The whiskers extend to the most extreme values (i.e. ±2.7 standard deviation coverage) not considered as outliers, and the outliers are plotted using the "+" symbol.

Similarly, four basis functions are investigated here, namely Empty, Constant, Linear, and Pure Quadratic, whose specifications are listed in Eqs. (5)–(8), respectively, where $B = (b(x_1),\ b(x_2), \ldots, b(x_n))^T$, $X = (x_1,\ x_2, \ldots, x_n)^T$, and $X^2 = \begin{pmatrix} x_{11}^2 & x_{12}^2 & \cdots & x_{1d}^2 \\ x_{21}^2 & x_{22}^2 & \cdots & x_{2d}^2 \\ \vdots & \vdots & \vdots & \vdots \\ x_{n1}^2 & x_{n2}^2 & \cdots & x_{\mathrm{n\,d}}^2 \end{pmatrix}$.

$$B = \text{Empty Matrix} \tag{5}$$

$$B = I_{n\times 1} \tag{6}$$

$$B = [1, X] \tag{7}$$

$$B = [1, X, X^2] \tag{8}$$

To estimate β, σ^2, and θ, the marginal log likelihood function in Eq. (9) is to be maximized, where $K(X, X|\theta)$ is the covariance function. The algorithm first computes $\hat{\beta}(\theta, \sigma^2)$, maximizing the log likelihood function with respect to β given θ and σ^2. It then obtains the β-profiled likelihood, $\log\{P(y|X, \widehat{\beta}\ (\theta, \sigma^2), \theta, \sigma^2)\}$, which is to be maximized over θ and σ^2 to compute their estimates.

$$\begin{aligned} \log P(y|X, \beta, \theta, \sigma^2) = & -\frac{1}{2}\{(y - B\beta)^T[K(X, X|\theta) + \sigma^2 I_n]^{-1}(y - B\beta)\} - \frac{n}{2}\log 2\pi \\ & -\frac{1}{2}\log |K(X, X|\theta) + \sigma^2 I_n| \end{aligned} \tag{9}$$

2.2. Performance evaluation

Performance of the proposed GPR models is evaluated using the root mean square error (RMSE), mean absolute error (MAE), and

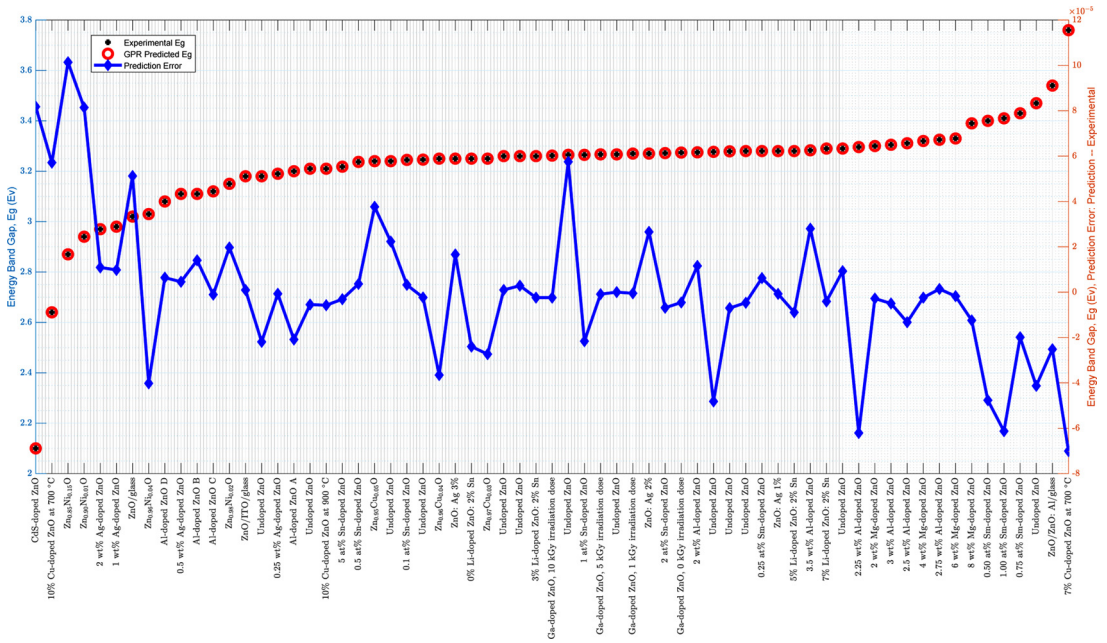

Fig. 3. The experimental vs. predicted E_g. The final GPR model is built using the whole sample with the Exponential kernel, Constant basis function, and standardized predictors. It has a log-likelihood of 21.8188, $\hat{\beta}$ of 3.1736, $\hat{\sigma}$ of 0.0021, $\hat{\sigma}_l$ of 0.2997, and $\hat{\sigma}_f$ of 0.2495. Detailed numerical predictions are listed in Table 1 (Column 6).

correlation coefficient (CC).

3. Empirical study

3.1. Description of dataset

The experimental data used, shown in Table 1 (Columns 1–5), are obtained from [1,3–6,9,11–14,18,19,23,25,29]. The dataset covers a wide range of ZnO films that are prepared through different synthesis methods and doped with various metal elements. The lattice parameters, a, and measured grain size are used as descriptors. E_g values are calculated using the Tauc relationship [44] after acquiring the transmittance data by the UV-VIS spectrometer in each reference in Table 1. A total of 65 ZnO films with the energy band gap, E_g, ranging from 2.100 eV to 3.760 eV are explored. Data visualization in Fig. 1 reveals nonlinear relationships, which are modeled through the GPR.

3.2. Computational methodology

MATLAB is utilized for computations and simulations in this work. The relationship between model performance and training data sizes is first investigated in Fig. 2, which shows the benefit of training the GPR using all observations. The stability of the GPR approach is confirmed by bootstrap analysis in Section 4.3.

4. Result and discussion

4.1. Prediction accuracy

The final GPR model is detailed in Fig. 3, which shows good alignment between predicted and experimental data. The CC, RMSE, and MAE are 99.99%, 0.00003134 (0.0010% of the average experimental E_g), and 0.00002053 (0.0006% of the average experimental E_g), respectively, representing good prediction performance.

4.2. Prediction stability

Given the relatively small sample size (see Table 1) used, the prediction stability of the GPR is assessed through bootstrap analysis in Fig. 4, which shows that the modeling approach maintains high CCs, low RMSEs, and low MAEs over the bootstrap samples. This result suggests that the GPR might be generalized for E_g modeling of ZnO films based on larger samples.

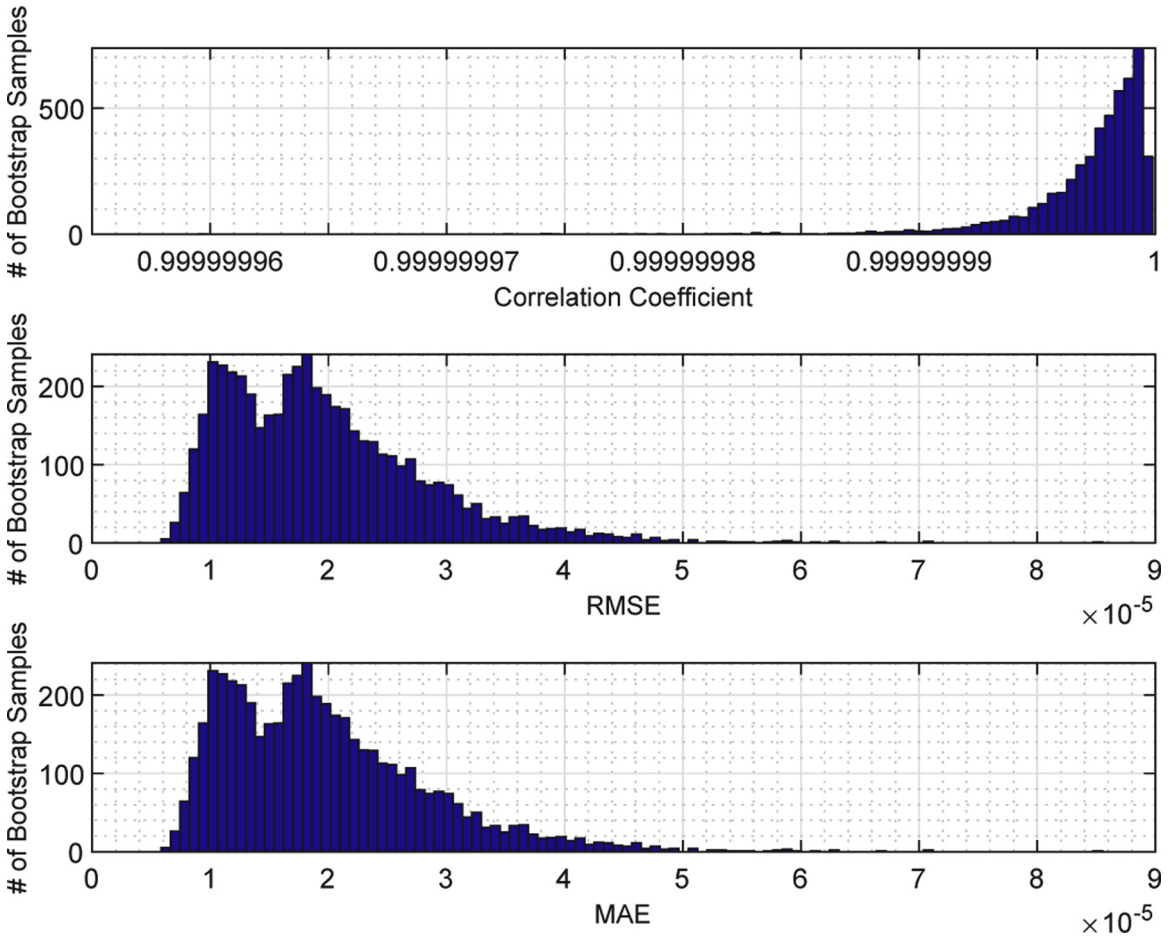

Fig. 4. Bootstrap analysis of GPR prediction stability. 5000 bootstrap samples are drawn with replacements from the whole sample. Each bootstrap sample is used to train the GPR based on the Exponential kernel, Constant basis function, and standardized predictors, and obtain the associate model performance. The histograms show distributions of the *CC*, *RMSE*, and *MAE* over the 5000 bootstrap samples, whose averages are 99.99%, 0.00001963, and 0.000011653, respectively.

Table 2
GPR prediction sensitivities to choices of kernels and basis functions.

Kernel	Basis Function	CC	RMSE	$\frac{\text{RMSE}}{\text{Samplemean}}$	MAE	$\frac{\text{MAE}}{\text{Samplemean}}$
Exponential	Constant	99.99%	0.00003134	0.0010%	0.00002053	0.0006%
Exponential	Empty	99.99%	0.00003969	0.0012%	0.00002538	0.0008%
Exponential	Linear	99.99%	0.00002976	0.0009%	0.00001954	0.0006%
Exponential	Pure quadratic	99.99%	0.00002964	0.0009%	0.00001869	0.0006%
Squared exponential	Constant	52.61%	0.17892816	5.5568%	0.09490542	2.9474%
Matern 5/2	Constant	99.99%	0.00339031	0.1053%	0.00174008	0.0540%
Rational quadratic	Constant	99.99%	0.00338039	0.1050%	0.00172936	0.0537%

Notes: The final GPR model is based on the exponential kernel and constant basis function, with standardized predictors.

4.3. Prediction sensitivity

Table 2 shows that the Exponential kernel is the optimal choice among kernels considered. With the Exponential kernel, prediction results are not sensitive to choices of basis functions. While the Constant basis function given the Exponential kernel leads to slightly worse model performance as compared to more complicated basis functions, such Linear and Pure Quadratic, it is selected as the final specification for its simplicity, which usually is a benefit to model generalization.

5. Conclusion

The Gaussian process regression (GPR) model is developed to predict the energy bandgap, E_g, of ZnO films based on the lattice parameters and grain size. The high correlation coefficient between the predicted and experimental E_g, the low prediction root mean square error and mean absolute error, and stable model performance suggest the usefulness of the GPR for modeling and understanding the relationship between structural and morphological parameters and E_g. This modeling approach is straightforward and simple, which requires fewer parameters as compared to many other modeling methods. The model applies to a wide range of undoped and doped-ZnO films made by various synthesis methods. As part of computational intelligence approaches, it could also be used to help design and understandings of multi-doped ZnO films with tunable E_g.

References

[1] A. Acharya, B. Sarwan, R. Panda, S. Shrivastava, V. Ganesan, Tuning of TCO properties of ZnO by silver addition, Superlattices Microstruct. 67 (2014) 97–109.
[2] A.N. Andriotis, M. Menon, Band gap engineering via doping: a predictive approach, J. Appl. Phys. 117 (2015) 125708.
[3] Y. Aoun, B. Benhaoua, S. Benramache, B. Gasmi, Effect of deposition rate on the structural, optical and electrical properties of zinc oxide (ZnO) thin films prepared by spray pyrolysis technique, Optik 126 (2015) 2481–2484.
[4] E. Asikuzun, O. Ozturk, L. Arda, C. Terzioglu, Preparation, growth and characterization of nonvacuum Cu-doped ZnO thin films, J. Mol. Struct 1165 (2018) 1–7.
[5] H. Aydin, H. El-Nasser, C. Aydin, A.A. Al-Ghamdi, F. Yakuphanoglu, Synthesis and characterization of nanostructured undoped and Sn-doped ZnO thin films via sol-gel approach, Appl. Surf. Sci. 350 (2015) 109–114.
[6] B. Benhaoua, A. Rahal, S. Benramache, The structural, optical and electrical properties of nanocrystalline ZnO:Al thin films, Superlattices Microstruct. 68 (2014) 38–47.
[7] T. Bretagnon, P. Lefebvre, T. Guillet, T. Taliercio, B. Gil, C. Morhain, Barrier composition dependence of the internal electric field in ZnO/Zn1-*x*MgxO quantum wells, Appl. Phys. Lett. 90 (2007) 201912.
[8] K.W. Chee, W. Guo, J.R. Wang, Y. Wang, Y. Chen, J. Ye, Tuning photonic crystal fabrication by nanosphere lithography and surface treatment of AlGaN-based ultraviolet light-emitting diodes, Mater. Des. 160 (2018) 661–670.
[9] S.C. Das, R.J. Green, J. Podder, T.Z. Regier, G.S. Chang, A. Moewes, Band gap tuning in ZnO through Ni doping via spray pyrolysis, J. Phys. Chem. C 117 (2013) 12745–12753.
[10] Y.Q. Fu, J. Luo, X. Du, A. Flewitt, Y. Li, G. Markx, A. Walton, W. Milne, Recent developments on ZnO films for acoustic wave based bio-sensing and microfluidic applications: a review, Sens. Actuators B: Chem. 143 (2010) 606–619.
[11] H. He, J. Fei, J. Lu, Sm-doping effect on optical and electrical properties of ZnO films, J. Nanostruct. Chem. 5 (2015) 169–175.
[12] K. Joshi, M. Rawat, S.K. Gautam, R. Singh, R. Ramola, F. Singh, Band gap widening and narrowing in Cu-doped ZnO thin films, J. Alloys Compd. 680 (2016) 252–258.
[13] M. Karyaoui, A. Mhamdi, H. Kaouach, A. Labidi, A. Boukhachem, K. Boubaker, M. Amlouk, R. Chtourou, Some physical investigations on silver-doped ZnO sprayed thin films, Mater. Sci. Semicond. Process. 30 (2015) 255–262.
[14] G. Kaur, A. Mitra, K. Yadav, Pulsed laser deposited Al-doped ZnO thin films for optical applications, Prog. Nat. Sci.: Mater. Int. 25 (2015) 12–21.
[15] L.Y. Liu, Z.X. Zhang, X.F. Gou, H.X. Yang, Molecular modelling of the effect of loading rate on elastic properties of CNT-polyethylene nanocomposite and its interface, Mater. Res. Express 6 (2020) 12502.
[16] S. Majumder, M. Jain, P. Dobal, R. Katiyar, Investigations on solution derived aluminium doped zinc oxide thin films, Mater. Sci. Eng. B 103 (2003) 16–25.
[17] A. Manzoli, M. Santos, S. Machado, A voltammetric and nanogravimetric study of ZnSe electrodeposition from an acid bath containing Zn (II) and Se (IV), Thin Solid Films 515 (2007) 6860–6866.
[18] M. Mekhnache, A. Drici, L.S. Hamideche, H. Benzarouk, A. Amara, L. Cattin, J. Bernede, M. Guerioune, Properties of ZnO thin films deposited on (glass, ITO and ZnO: Al) substrates, Superlattices Microstruct. 49 (2011) 510–518.
[19] M.N.H. Mia, M.F. Pervez, M.K. Hossain, M.R. Rahman, M.J. Uddin, M.A. Al Mashud, H.K. Ghosh, M. Hoq, Influence of Mg content on tailoring optical bandgap of Mg-doped ZnO thin film prepared by sol-gel method, Results Phys. 7 (2017) 2683–2691.
[20] B.C. Mohanty, Y.H. Jo, D.H. Yeon, I.J. Choi, Y.S. Cho, Stress-induced anomalous shift of optical band gap in ZnO:Al thin films, Appl. Phys. Lett. 95 (2009) 062103.
[21] M. Oshikiri, F. Aryasetiawan, Band gaps and quasiparticle energy calculations on ZnO, ZnS, and ZnSe in the zinc-blende structure by the GW approximation, Phys. Rev. B 60 (1999) 10754.
[22] S.D. Ponja, S. Sathasivam, I.P. Parkin, C.J. Carmalt, Highly conductive and transparent gallium doped zinc oxide thin films via chemical vapor deposition, Sci. Rep. 10 (2020) 1–7.
[23] A. Rherari, M. Addou, M. Haris, Structural and optical characterization of (Sn/Li) co-doped ZnO thin films deposited by spray pyrolysis technique, J. Mater. Sci.: Mater. Electron. 28 (2017) 15762–15767.
[24] J. Schwartz, C.C. Koch, Y. Zhang, X. Liu. Formation of bismuth strontium calcium copper oxide superconductors. US Patent US9773962B2 (September 26, 2017).
[25] F.J. Serrao, K. Sandeep, S. Bhat, S. Dharmaprakash, High energy electron irradiation effects on Ga-doped ZnO thin films for optoelectronic space applications, Appl. Phys. A 124 (2018) 224.
[26] T. Shen, G. Li, C. Cheng, Y. Zhao, Doping effects of carbon and titanium on the critical current density of MgB2, Supercond. Sci. Technol. 19 (2006) 1219.
[27] A. Tsukazaki, A. Ohtomo, T. Onuma, M. Ohtani, T. Makino, M. Sumiya, K. Ohtani, S.F. Chichibu, S. Fuke, Y. Segawa, et al., Repeated temperature modulation epitaxy for p-type doping and light-emitting diode based on ZnO, Nat. Mater. 4 (2005) 42–46.
[28] S. Venkatachalam, D. Mangalaraj, S.K. Narayandass, K. Kim, J. Yi, Structure, optical and electrical properties of ZnSe thin films, Physica B: Condensed Matter 358 (2005) 27–35.
[29] A.K. Vishwakarma, L. Yadava, Fabrication and characterization of CDS doped ZnO nano thick films, Vacuum 155 (2018) 214–218.
[30] Y. Wang, M. Li, D. Hasanyan, J. Gao, J. Li, D. Viehland, Geometry-induced magnetoelectric effect enhancement and noise floor reduction in Metglas/piezofiber sensors, Appl. Phys. Lett. 101 (2012) 092905.
[31] C. Xia, F. Wang, C. Hu, Theoretical and experimental studies on electronic structure and optical properties of Cu-doped ZnO, J. Alloys Compd. 589 (2014) 604–608.
[32] Y. Xiao, X.F. Gou, D.G. Zhang, A one-dimension nonlinear hysteretic constitutive model with elasto-thermo-magnetic coupling for giant magnetostrictive materials, J. Magn. Magn. Mater. 441 (2017) 642–649.
[33] Z. Yang, Z. Liu, J. Sheng, W. Guo, Y. Zeng, P. Gao, J. Ye, Opto-electric investigation for Si/organic heterojunction single-nanowire solar cells, Sci. Rep. 7 (2017) 1–9.
[34] Y. Zhang, S. Johnson, G. Naderi, M. Chaubal, A. Hunt, J. Schwartz, High critical current density $Bi_2Sr_2CaCu_2O$ *x*/Ag wire containing oxide precursor synthesized from nano-oxides, Supercond. Sci. Technol. 29 (2016) 095012.
[35] Y. Zhang, C.C. Koch, J. Schwartz, Synthesis of $Bi_2Sr_2CaCu_2Ox$ superconductors via direct oxidation of metallic precursors, Supercond. Sci. Technol. 27 (2014) 055016.
[36] Y. Zhang, C.C. Koch, J. Schwartz, Formation of $Bi_2Sr_2CaCu_2O$ *x*/Ag multifilamentary metallic precursor powder-in-tube wires, Supercond. Sci. Technol. 29 (2016) 125005.
[37] Y. Zhang, X. Xu, Machine learning modeling of lattice constants for half-Heusler alloys, AIP Adv. 10 (2020) 045121.

[38] Y. Zhang, X. Xu, Machine learning the magnetocaloric effect in manganites from compositions and structural parameters, AIP Adv. 10 (2020) 035220.
[39] Y. Zhang, X. Xu, Machine learning the magnetocaloric effect in manganites from lattice parameters, Appl. Phys. A 126 (2020) 341.
[40] Y. Zhang, X. Xu, Predicting doped MgB_2 superconductor critical temperature from lattice parameters using Gaussian process regression, Physica C: Supercond. Appl. 573 (2020) 1353633.
[41] Y. Zhang, X. Xu, Predicting the thermal conductivity enhancement of nanofluids using computational intelligence, Phys. Lett. A 384 (2020) 126500.
[42] Y. Zhang, X. Xu, Yttrium barium copper oxide superconducting transition temperature modeling through Gaussian process regression, Comput. Mater. Sci. 179 (2020) 109583.
[43] Y.G. Zhang, G.B. Zhang, Y. Xu Wang, First-principles study of the electronic structure and optical properties of Ce-doped ZnO, J. Appl. Phys. 109 (2011) 063510.
[44] Y. Zhao, Y. Jiang, Y. Fang, The influence of substrate temperature on ZnO thin films prepared by PLD technique, J. Cryst. Growth 307 (2007) 278–282.